Extrusion-Spheronization of UiO-66 and UiO-66_NH$_2$ into Robust-Shaped Solids and Their Use for Gaseous Molecular Iodine, Xenon, and Krypton Adsorption

Alla Abramova, Nelly Couzon, Maëva Leloire, Philippe Nerisson, Laurent Cantrel, Sébastien Royer, Thierry Loiseau, Christophe Volkringer, and Jérémy Dhainaut*

Cite This: https://doi.org/10.1021/acsami.1c21380

Read Online

ACCESS | ⅈ Metrics & More | 📰 Article Recommendations | 🆂ⅈ Supporting Information

ABSTRACT: The use of an extrusion-spheronization process was investigated to prepare robust and highly porous extrudates and granules starting from UiO-66 and UiO-66_NH$_2$ metal−organic framework powders. As-produced materials were applied to the capture of gaseous iodine and the adsorption of xenon and krypton. In this study, biosourced chitosan and hydroxyethyl cellulose (HEC) are used as binders, added in low amounts (less than 5 wt % of the dried solids), as well as a colloidal silica as a co-binder when required. Characterizations of the final shaped materials reveal that most physicochemical properties are retained, except the textural properties, which are impacted by the process and the proportion of binders (BET surface area reduction from 5 to 33%). On the other hand, the mechanical resistance of the shaped materials toward compression is greatly improved by the presence of binders and their respective contents, from 0.5 N for binderless UiO-66 granules to 17 N for UiO-66@HEC granules. UiO-66_NH$_2$-based granules demonstrated consequent iodine capture after 48 h, up to 527 mg/g, in line with the pristine UiO-66_NH$_2$ powder (565 mg/g) and proportionally to the retaining BET surface area (−5% after shaping). Analogously, the shaped materials presented xenon and krypton sorption isotherms correlated to their BET surface area and high predicted xenon/krypton selectivity, from 7.1 to 9.0. Therefore, binder-aided extrusion-spheronization is an adapted method to produce shaped solids with adequate mechanical resistance and retained functional properties.

KEYWORDS: metal−organic frameworks, extrusion-spheronization, shaping, iodine capture, Xe/Kr separation

■ INTRODUCTION

Currently, the nuclear industry provides about 10% of the world's electricity through 445 power reactors, making it the fourth source of electricity production behind coal (38%), natural gas (23%), and hydroelectricity (16%). While the number of power plants remained somehow constant since 1996, about 50 new reactors are under construction. Recently, the European Commission declared nuclear energy as sustainable. Hence, a consequent research and development effort is devoted to the continuous improvement of the safety of power reactors, sustainability of electricity production, and long-term waste management. Besides, novel solutions to valorize fission products or to limit the effects of potential nuclear plant accidents are desirable.

For instance, in the case of a nuclear meltdown, as occurred in 2011 at Fukushima Daiichi nuclear power plant, venting should be done to avoid containment overpressurization,[1] which could cause irremediable structural damage and further release of radioactive material with widespread effects—as it happened.[2] However, the vented steam contains a significant concentration of volatile radionuclides and especially iodine-131 which is a major radionuclide comprising about 3 wt % of the total fission products from uranium neutron reactions.[1] Importantly, ^{131}I released in the environment can be either inhaled or ingested through food products (vegetables, dairy farms, etc.) and penetrate the thyroid tissues, increasing the incidence of thyroid cancers as observed following the Chernobyl disaster.[3]

To minimize the release of radionuclides, and hence their consequences on the health and the environment, passive filtration systems have been developed by the nuclear industry to treat the vented contaminated steam. Especially, filtered containment venting systems (FCVS), either based on the use

of a scrubber (wet FCVS) or solid filter (dry FCVS), allow us to trap above 99% of molecular iodine but are much less efficient for organic iodide species.[1,4] The capture of these organics can be performed using a fixed bed of silver-doped zeolites, which is typically installed downstream of the first filtration step.[4] For instance, up to 455 mg of molecular iodine can be captured with a gram of silver-doped ZSM-5 zeolite.[5] However, the zeolite trapping capacities with respect to iodine derivatives such as CH_3I may be inhibited by gaseous contaminants (mainly CO).[6] Thus, to further improve the FCVS efficiency, an alternative approach can be to study the trapping properties of innovative porous material with similar or higher adsorption capacities toward iodine species and exhibiting larger pores.[7] Of note, the material should be stable at 140 °C under steam and irradiation, related to the typical conditions occurring in a vented contaminated steam.[8] Activated carbons impregnated with triethylenediamine (TEDA) have been applied for I_2 and CH_3I capture. They present long-term performance under simulated operating conditions, with up to 99% of the CH_3I retained after 15 months.[9] However, they exhibit a low autoignition temperature, which makes them unsafe to use in the nuclear field.[7] Metal−organic frameworks (MOFs) have been studied from 2011, first using the Zn-based ZIF-8 MOF, which possesses pores of size adequate for molecular iodine ($I_{2\,kinetic\ diameter}$ = 5 Å).[10] A major breakthrough was reported with MOFs presenting electron donor groups attached to organic linkers since their presence leads to the polarization of the electron cloud of molecular iodine.[11] Iodine loadings above 500 mg per gram of MOF can be obtained,[12] with a record uptake of 2.79 g/g.[13]

While iodine-131 represents one of the major gaseous fission products, every fission event also produces 0.25 to 0.30 atom of valorizable noble gas species including xenon and krypton elements, with Xe atoms being seven times more likely to be produced than Kr atoms.[14] The process off-gas containing the noble gas species as well as ^{129}I, $^{14}CO_2$, $^{3}H_2O$, and NO_x are usually vented to the atmosphere, which could arise hazardous problematics. On the other hand, xenon is extremely scarce in the Earth's atmosphere (about 87 ppb),[15] making it the most expensive noble gas to purchase, while it has a number of key applications, especially in the medical, lighting, and electronic fields. Hence, it is of utmost importance to develop novel ways to capture radioactive components from the process off-gas and produce high-purity Xe gas. In this line, many porous solids have been applied to the separation of xenon over krypton. Activated carbons present interesting xenon uptakes but low Xe/Kr selectivity, between 2 and 3.[16] Moreover, the presence of NO_x in the process off-gas forbids their use due to possible fire hazards. On the other hand, zeolites show remarkable Xe/Kr selectivity, over 4, but only limited noble gas uptakes.[17] Of note, silver-doped zeolites gave rise to higher xenon uptakes and Xe/Kr selectivity than their protonated form.[18] MOFs, presenting some of the highest xenon uptakes and Xe/Kr selectivities,[15] are hence promising materials for this application. The SBMOF-1 compound is one of the current leading materials for separation, with a Xe/Kr selectivity of 16 owing to its pores closely matching the size of xenon atoms.[19] The record for xenon uptake in a MOF was obtained with the PCN-14 compound, having a xenon uptake of 7.1 mmol/g, 50% higher than the best activated carbon.[20]

MOFs are hybrid crystalline materials whose structure results from the assembly of metallic nodes (clusters or ions) with multitopic organic linkers through coordination bondings. Their strength lies in this modular nature, as most of their physicochemical properties can be tailored for specific applications. This resulted in the report of over 10.000 MOF structures within the last 20 years, with several prototypal MOFs presenting surface areas (S_{BET}) over 1.000 m^2/g and pore sizes up to 98 Å.[21] Owing to these properties, selected MOFs demonstrate excellent performances in adsorption, catalysis, and separation applications.[21] On the downside, their structure is rarely stable above 300 °C in air (thermal decomposition) or in aqueous phase (hydrolysis of the coordination bonds).[22] For commercial applications, MOF structures based on trivalent metals or above, less prone to hydrolysis, should be preferred.

The $[Zr_6O_4(OH)_4(O_2C\text{-}C_6H_4\text{-}CO_2)_6]$ MOF structural archetype, also known as UiO-66, has been widely investigated owing to its good stability against moisture, related to the coordination of hexanuclear $Zr_6O_4(OH)_4$ clusters with up to 12 terephthalate linkers, and high adsorption capacity, in line with its BET surface area exceeding 1.000 m^2/g.[23] Moreover, the UiO-66 MOF presents a pore size distribution typically between 8 and 11 Å, due to the presence of defects in its structure.[23] Starting from the structural archetype, several substructures can be obtained, either by changing the metal (Hf, Ce, Th, U, Np, etc.) or the organic linker (fumarate: UiO-66-FA, biphenyldicarboxylate: UiO-67, etc.) or even by adding organic functionalities to the terephthalate linkers (UiO-66_NH_2, UiO-66_OH, UiO-66_COOH, etc.).[24−27]

Owing to their good stability and scalable synthesis, this family of MOFs has been used for the capture of a broad array of molecules in gas and liquid phases,[28] including I_2.[29] In particular, UiO-66_NH_2 has been applied for the capture of substantial amounts of NO_2,[30] HCl and Cl_2,[31] and CO_2,[32] owing to their high binding energy with the electro-donor amino groups. Recently, our group applied this MOF for the immobilization of 131-iodine under simulated nuclear accidental conditions.[8] UiO-66_NH_2 millimetric granules were preloaded with 7.8 mg of $^{131}I_2$ per gram of MOF and further subjected to a continuous wet air flow with a relative humidity of 25%, an absolute pressure of 3.5 bar and a temperature of 120 °C.[8] Moreover, a γ radiation dose rate of 1.9 kGy/h was applied. After 30 h under these severe nuclear accidental conditions, no leakage of $^{131}I_2$ was detected and the UiO-66_NH_2 structure remained intact. Thus, this MOF candidate is promising for applications linked to fission products mitigation in a nuclear accident context.

However, one of the limits of this study is the weak mechanical resistance of the binderless granules used, below 1 Newton. In a fixed bed, the solids are subjected to friction and/or abrasion, which will produce fine particles in the case of low mechanical resistance and will clog the filters typically installed downstream of the fixed bed over time. This in turn would dangerously arise the pressure within the installation. More generally, MOFs shaping remains a major bottleneck prior to their wider use in the everyday life due to several reasons: (1) MOFs cannot undertake sintering, which is typically used to reinforce inorganic materials, due to their mild thermal resistance (typically below 300 °C); (2) the use of a large amount of binders significantly lowers their performances, making them less attractive compared to activated carbons and zeolites; and (3) most MOF structures are not rigid enough to withstand high compression pressure or shearing force, as reached when using pelletization, extrusion, or granulation

processes.[33] However, it was reported that the UiO-66-based MOFs offer an adequate resistance for binderless pelletization,[34] but the resulting pellets are not suited for a fixed-bed application due to the resulting spatial heterogeneities. More suited solids for fixed beds include extrudates and granules, giving the best compromise between pressure drop, contact surface, and filling ratio. UiO-66 and UiO-66_NH$_2$ compounds have been previously shaped under the granules form in the presence of binders,[35−37] allowing us to obtain relatively resistant shaped bodies at the expense of the porosity. Another derivative, UiO-66_COOH, has been shaped following extrusion, in the presence of a silicon resin, which greatly affected the resulting porosity (S_{BET} = −40% with 5.5 wt % of silicon resin).[38] Intriguingly, no extrusion of UiO-66 nor UiO-66_NH$_2$ has been reported so far.

Hence, the following study is devoted to the preparation of robust and highly porous extrudates and granules made of UiO-66 and UiO-66_NH$_2$ compounds. For this purpose, a few percentages of a biosourced binder, either derived from cellulose or chitosan, are added to a MOF-based paste prior to extrusion. The extrudates were characterized as such or further spheronized to produce granules. This is the first time that an extrusion-spheronization process is applied to a MOF-based material. The I_2 adsorption capacity of these granules was evaluated using a specific testing bench. Notably, chitosan possesses inherent amino functions, which could either improve or at least make the effect of the presence of binder mild on the I_2 uptake of the resulting composite. Finally, Xe and Kr sorption isotherms of these composites were also measured at room temperature to diversify their possible applications for the nuclear energy field and the valorization of xenon gas.

■ EXPERIMENTAL SECTION

Reagents: *N,N*-dimethylformamide (DMF, Carlo Erba 99.9%), methanol (MeOH, VWR 98.5+ %), zirconium tetrachloride (ZrCl$_4$, Acros Organics 98%), acetic acid (CH$_3$COOH, VWR 99+ %), formic acid (HCOOH, Acros Organics 98%), terephthalic acid (H$_2$BDC, Alfa Aesar 98%), 2-aminoterephthalic acid (H$_2$BDC-NH$_2$, Aldrich 99%), 2-hydroxyethyl cellulose (HEC, Aldrich M_w = 1 300 000 g/mol), deacetylated chitin (chitosan, Aldrich M_w = 310 000 to 375 000 g/mol), Ludox HS-40 (colloidal silica, Sigma-Aldrich, 40%), potassium iodide (KI, Alfa Aesar 99%). All reagents were used without further purification.

Synthesis of UiO-66. Its preparation was based on the scale-up synthesis protocol described elsewhere.[5] Briefly, 3 L of DMF, 40 g of ZrCl$_4$ (+150 mL of DMF for rinsing), 56 g of H$_2$BDC (+100 mL of DMF for rinsing), and 0.65 L of HCOOH were added successively in a mechanically stirred, 8 L stainless steel autoclave. The latter was sealed, and the starting reactants were mixed at 100 rounds per minute (rpm) for 24 h at 120 °C. After cooling down the autoclave, the mixture was collected and the resulting solid was separated from the supernatant by centrifugation at 4000 rpm for 10 minutes. The solid was then dispersed twice for 24 h in fresh DMF and three times in MeOH, with separation by centrifugation in-between. Finally, the white powdered product was dried for 1 h at 100 °C and then for 8 h at 150 °C. Final yield = 65 mol % upon Zr.

Synthesis of UiO-66_NH$_2$. A similar protocol was used, with slightly different weights of the starting chemical reactants but identical reaction conditions. More specifically, 80 g of ZrCl$_4$ and 120 g of H$_2$BDC-NH$_2$ were added in the 8 L autoclave. Final yield = 85 mol % upon Zr.

Extrusion-Spheronization of UiO-66 and UiO-66_NH$_2$ Solids. All steps were conducted using a Caleva Multi Lab apparatus. First, a MOF-based paste was formed by kneading about 10 g of powdered MOF (either UiO-66 or UiO-66_NH$_2$) with about 12 g of

a gel containing the binder (either 2-hydroxyethyl cellulose—HEC—or deacetylated chitin—chitosan) at 150 rpm for 30 min. When using HEC as a binder with UiO-66 powder, a second batch composition was obtained by adding 0.47 g of a silica suspension. The exact composition of the pastes as well as the protocol to prepare gels are given in the SI. Successive additions of portions of the MOF powder gave better paste homogeneity. The paste was recovered and pushed into the feed zone of a single-screw extruder rotating at 90 rpm. At the end of the screw, a die with multiple holes of diameter 1 mm was fitted. The as-obtained extrudates (Figure S1) were dried overnight at 120 °C.

For the production of granules, 1.5 g of as-obtained extrudates was directly placed onto the 3 mm pitch plate of the spheronization module. The plate was rotated at 2500 rpm for 10 minutes. After sieving (mesh size 500 μm), 1.2 to 1.4 g of rounded granules was obtained. The granules were also dried overnight at 120 °C.

All solids are named according to their MOF structure and the binder used, following the denomination MOF@binder related to the samples: UiO-66@HEC, UiO-66@chitosan, UiO-66_NH$_2$@HEC, UiO-66_NH$_2$@chitosan, and UiO-66@HEC-Ludox.

Characterization. Powder X-ray diffraction patterns (XRD) were collected on a Bruker D8 Advanced AXS diffractometer equipped with Cu K$_{\alpha 1}$ monochromatic radiation source (λ = 1.5418 Å) and operated at 40 kV and 30 mA. X-ray diagrams were recorded within the 5−50° region with a 0.02° step size (step time = 0.5 s). Nitrogen sorption isotherms at 77 K were measured with a Micromeritics Tristar II Plus apparatus. Prior to measurement, the samples were degassed for 8 h at 150 °C. The surface area (S_{BET}) was determined by applying the multipoint B.E.T. algorithm over a linear portion at relative pressures in the range 0.04−0.25. The micropore and total pore volumes were estimated from the adsorbed volume of nitrogen at relative pressures of 0.25 and 0.99, respectively. Scanning electron microscopy (SEM) images were taken using a JEOL JSM 6700F. The solids were directly deposited on a carbon tape, and electron conductivity was obtained by depositing silver lacquer. ImageJ (v.1.52a) was used to determine the crystal size distribution from SEM micrographs. Thermogravimetric analyses (TGA) were conducted with a Mettler Toledo TGA/DSC 3+ thermal analyzer over the range 25−600 °C under air flow (80 mL/min), following a heating rate of 2 °C·min^{-1}. Fourier transform infrared (FTIR) spectra were recorded at room temperature between 4000 and 400 cm^{-1} using a PerkinElmer Spectrum Two Spectrometer equipped with an ATR sampling module. The deacetylation degree (DD) of the commercial chitosan was evaluated following the equation DD = 1 − $(A_{1320}/A_{1420}$ − 0.3822)/3.133.[39] The averaged bulk density was determined by weighing 10 dried extrudates and measuring their dimensions with a digital caliper. The compressive strength of the solids was determined by a Vinci Technologies Versatile Crushing Strength Tester, using a set of flat anvil and hammer. The load applied was recorded by the force sensor as a function of the displacement of the punch at a constant speed of 0.6 mm/min until failure, happening at the ultimate crushing strength of the solid (called compressive strength hereafter for simplicity). For each sample, 10 representative solids were crushed and the resulting compressive strength values, given in Newton, were averaged. Xenon and krypton sorption isotherms at 293.15 ± 2 K were measured separately with a Micromeritics ASAP 2020 PLUS. Prior to measurement, the samples were degassed for 8 h at 120 °C. Xe/Kr selectivity is determined from the ratio of Henry's constants, which are obtained from the slope of the isotherms in a linear, low-pressure range (p/p_0 < 0.03).

Iodine Capture Test. The adsorption capacity of the investigated MOF-based granules toward I_2 was investigated using a dedicated experiment.[12] The experimental setup devoted to the I_2 sorption test can be divided into three main parts: generation of the I_2 inlet flow, a fixed-bed glass reactor, and the quantification system composed of bubblers containing potassium iodide solution (KI, 0.1 M) and a UV−vis spectrometer (Figure S2). Gaseous iodine is produced from the sublimation process (0.2 mg/h) of crystalline iodine beads in a permeation chamber (VICI Metronics, Inc., Dynacalibrator Model 150) set at 100 °C and is carried by a controlled flow of argon (10
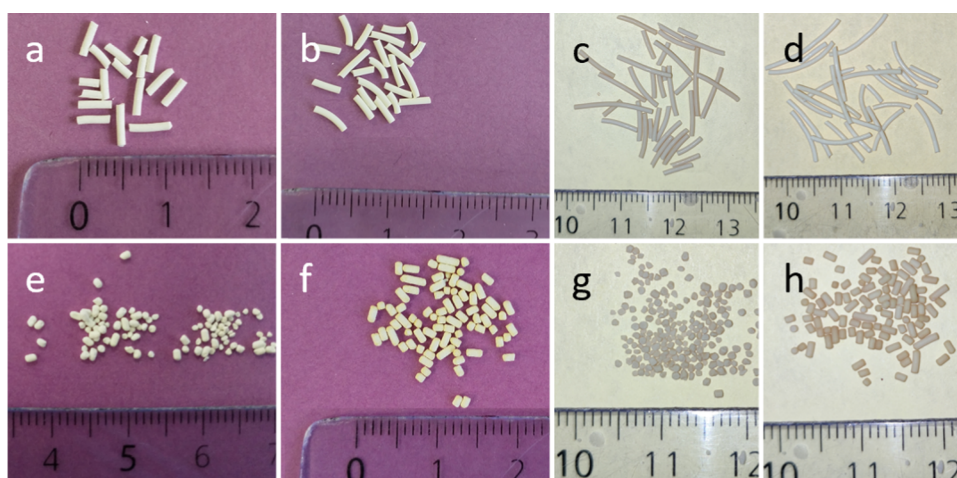
Figure 1. Photographs of (a−d) extrudates and (e−h) granules of (a, e) UiO-66@HEC, (b, f) UiO-66@chitosan, (c, g) UiO-66_NH$_2$@HEC, and (d, h) UiO-66_NH$_2$@chitosan.
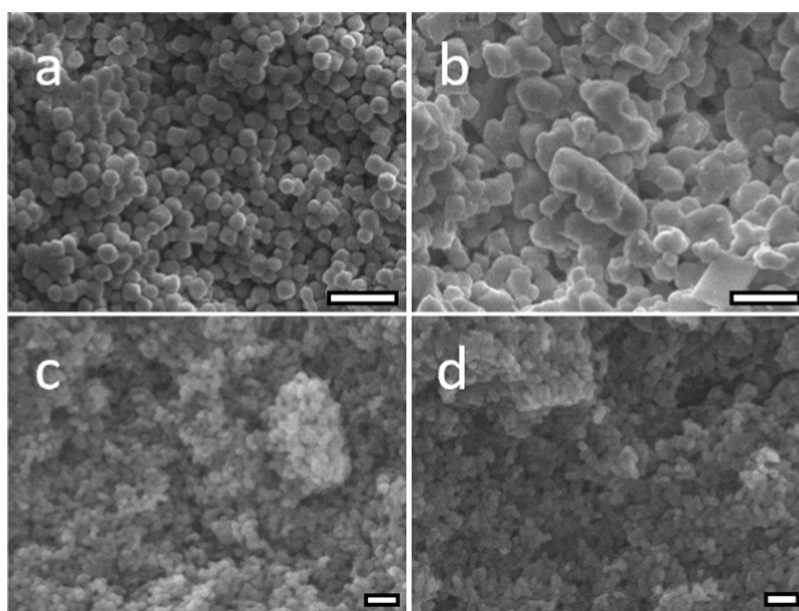

Figure 2. SEM micrographs of extrudates made with (a) UiO-66@HEC, (b) UiO-66@chitosan, (c) UiO-66_NH$_2$@HEC, and (d) UiO-66_NH$_2$@chitosan. Scale bars: (a, b) 1 μm and (c, d) 100 nm.

nL/h; $[I_2]$ = 100 ppm) and then, transferred into the glass sintered cell (4 mm diameter) at room temperature (20 ± 1 °C) through an inert PTFE line.

The quantity of iodine passing through the glass sintered cell (*i.e.,* not adsorbed by the granules) is collected in a bubbler held in a 2 L opaque flask of 0.1 M KI solution, leading to the quantitative formation of the triiodide ion I_3^-. A peristaltic pump allows the continuous flow of the solution through the quartz cell of a UV−vis spectrometer, and the concentration of I_3^- generated in the bubbler is measured every 4 min at the absorbance of the selected band (λ_{max} = 352 nm). The kinetic adsorption of iodine is then calculated from the difference between a blank curve (*i.e.,* no adsorbing material) and the curve collected in the presence of the granules in the reactor. The content of molecular iodine trapped within the porous framework is then calculated by means of a calibration curve.

Prior to analysis, MOF-based granules were thermally treated *ex situ* overnight at 120 °C to remove entrapped species within the pores. Activated UiO-66-based materials (20 mg) were transferred into the glass sintered cell, leading to a 1 cm bed height. The estimated residence time is about 0.04 s.

RESULTS AND DISCUSSION

Impact of Shaping on the Properties of UiO-66/UiO-66_NH$_2$. After extrusion and spheronization, and as observed in Figures 1 and S1, all shaped materials are dust-free and their aspect is homogeneous. The diameter of all extrudates and granules comprised between 0.89 and 0.96 mm, while the length of the granules seems related to the resistance of the extrudates toward attrition, and hence to the nature of the binder. Indeed, starting from extrudates with comparable lengths, UiO-66@chitosan and UiO-66_NH$_2$@chitosan are spheronized into 1.88 and 1.63 mm rounded granules, respectively, while UiO-66@HEC and UiO-66_NH$_2$@HEC lead to spherical solids (length = 0.9−1.2 mm). Several authors have shown that the spheronization mechanism,[40] which is based on abrasion, typically includes several stages: starting from extrudates, cylinders with rounded ends are produced first. Then, dumbbell-like solids are formed that are further split into ellipsoidal objects. Finally, spheres are obtained.

Table 1. Textural Properties, Average Compressive Strength (σ), Averaged over 10 Samples, and Estimated Binder Content (from TGA) of the MOF@binder Extrudate and Granule Series

sample	shape	S_{BET} (m²/g)	V_μ (cm³/g)	V_{meso} (cm³/g)	V_{meso} (%)	V_{tot} (cm³/g)	σ (N)	binder (wt %)
UiO-66	powder	1510 (100%)	0.59	0.04	6	0.63		
UiO-66@HEC	extrudate	941 (62%)	0.38	0.07	16	0.45	7.23 ± 1.47	2.7
	granule	1006 (67%)	0.38	0.13	25	0.51	1.64 ± 0.88	
UiO-66@chitosan	extrudate	1212 (80%)	0.47	0.03	6	0.50	19.45 ± 4.68	4.2
	granule	1291 (85%)	0.52	0.06	10	0.58	16.88 ± 7.65	
UiO-66_NH$_2$	powder	925 (100%)	0.39	0.30	43	0.69		
UiO-66_NH$_2$@HEC	extrudate	855 (92%)	0.35	0.68	66	1.03	14.59 ± 4.62	1.5
	granule	683 (74%)	0.28	0.46	62	0.74	11.32 ± 3.25	
UiO-66_NH$_2$@chitosan	extrudate	868 (94%)	0.35	0.72	67	1.07	13.22 ± 3.81	2.4
	granule	878 (95%)	0.36	0.55	60	0.91	8.62 ± 4.10	

Thus, different shapes come from a different stage reached for a similar amount of mechanical energy provided.

At the microscopic scale, several features can be observed. Notably, the initial UiO-66 and UiO-66_NH$_2$ powders, prepared under the same conditions, are composed of crystallites with different sizes and shapes as observed in Figure S3. UiO-66 crystals present a typical octahedral shape with an average diameter of 220 nm, while UiO-66_NH$_2$ crystals are smaller (78 nm) and less faceted. The packing density of a material is a function of the particles size distribution and their average size and shape.[41] Thus, UiO-66_NH$_2$-based solids might exhibit higher packing densities, which in turn would allow reaching higher volumetric uptakes and compressive strength. UiO-66@chitosan and UiO-66_NH$_2$@chitosan extrudates present averaged bulk densities of 0.87 and 0.86 g/cm³, respectively. These values are close to the reported value of 0.79 g/cm³ for MI-101(Cr) extrudates and higher than UiO-66 and UiO-66_NH$_2$ solids made by granulation (0.67 and 0.56 g/cm³, respectively).[35,42] Hence, the bulk density of extrudates is rather dictated by the extrusion process parameters including the inlet flowrate, die pressure, screw speed, and torque.[43] On the contrary, the crystallites size and shape do not seem to have a marked effect on the bulk density of the materials.

Figures 2 and S4 represent SEM micrographs of extrudates and granules prepared from UiO-66 and UiO-66_NH$_2$ powders, respectively. All solids present a dense packing of MOF crystallites, and no difference can be observed between extrudates and granules, revealing that the spheronization process has no impact at the microscopic scale. However, in the case of UiO-66, significant differences are observed depending on the nature of the binder. When the HEC gel is used, rounded instead of faceted crystals are observed. This could be due to the binder preferentially covering the crystal facets. More intriguingly, the use of the chitosan gel results in the formation of ill-defined and partially agglomerated particles. Individual UiO-66 crystals can still be observed, but most crystals seem to be incorporated within these bigger particles. In the case of UiO-66_NH$_2$-based solids, however, the crystals retained their shape and size and binders cannot be observed.

The surface and cross section of representative extrudates and granules were also observed by SEM and are displayed in Figures S5 (UiO-66@chitosan) and S6 (UiO-66_NH$_2$@ HEC), arbitrarily chosen as representative solids. Linear microgrooves can be observed over the surface of smooth extrudates (Figures S5.a and S6.a) and are due to the high pressure exerted within the die holes. On the other hand, the

surface of the granules (Figures S5.c and S6.c) is highly fractured and rough, due to the strong attrition exerted during spheronization. In both cases, the solids are homogeneously dense over their cross section.

Thermogravimetric curves of the MOF@binder extrudate series (MOF = UiO-66 and UiO-66_NH$_2$; binder = HEC or chitosan), displayed in Figure S7, were obtained under air and compared to their powder counterparts. The first weight loss, below 150 °C, is typically due to the desorption of weakly physisorbed water molecules. A second weight loss, between 150 and 350 °C, corresponds to the dehydroxylation of the MOF and the possible remaining DMF entrapped within the porosity,[44] as well as the combustion of organic binders. As the organic binders (HEC and chitosan) are thermally decomposed from 250 °C, the solids present lower thermal stabilities than their MOF powder counterparts. It remains significantly above 140 °C, which is the typical temperature reached inside FCVS.[8] Also, as the BDC_NH$_2$ organic linker starts degrading from around 300 °C, it is not possible to clearly evaluate its weight loss under these conditions. Importantly, by subtracting the varying amount of weakly physisorbed water, it is possible to roughly estimate the binder content in the extrudates, reported in Table 1. The provisional 3 wt % content is mostly respected for most extrudates (2.4−4.2 wt %), except UiO-66_NH$_2$@HEC, which is lower than expected (1.5 wt %). It is noticed that a lower binder content should improve the textural properties of the final material but will also induce lower mechanical resistance.

The powder X-ray diffractograms of the MOF@binder extrudate and granule series are given in Figure S8. All solids exhibit a PXRD pattern with well-defined Bragg peaks, and hence a crystalline structure, matching with the initial UiO-66 or UiO-66_NH$_2$ powder counterpart. An additional small hump around 8.7° (2θ) can be observed on the PXRD patterns of UiO-66@chitosan solids (see the inset in Figure S8.b), which can be attributed to the binder. To verify this hypothesis, the PXRD pattern of the commercial chitosan is displayed in Figure S9.a. A diffraction peak at 9.5° (2θ), ascribed to the (020) crystallographic plane of chitin,[45] is clearly observed. Chitosan is obtained from the deacetylation of chitin, the latter remaining as an impurity. To evaluate the actual content of chitin within the commercial chitosan, its FTIR spectrum was measured and is shown in Figure S9.b. The deacetylation degree (DD) of the commercial chitosan is estimated to be 68%, meaning that chitin represents more than 1 wt % of the UiO-66@chitosan solids.[39] This hump is not visible on the UiO-66_NH$_2$@chitosan solids, owing to its lesser content. Thus, the extrusion and spheronization
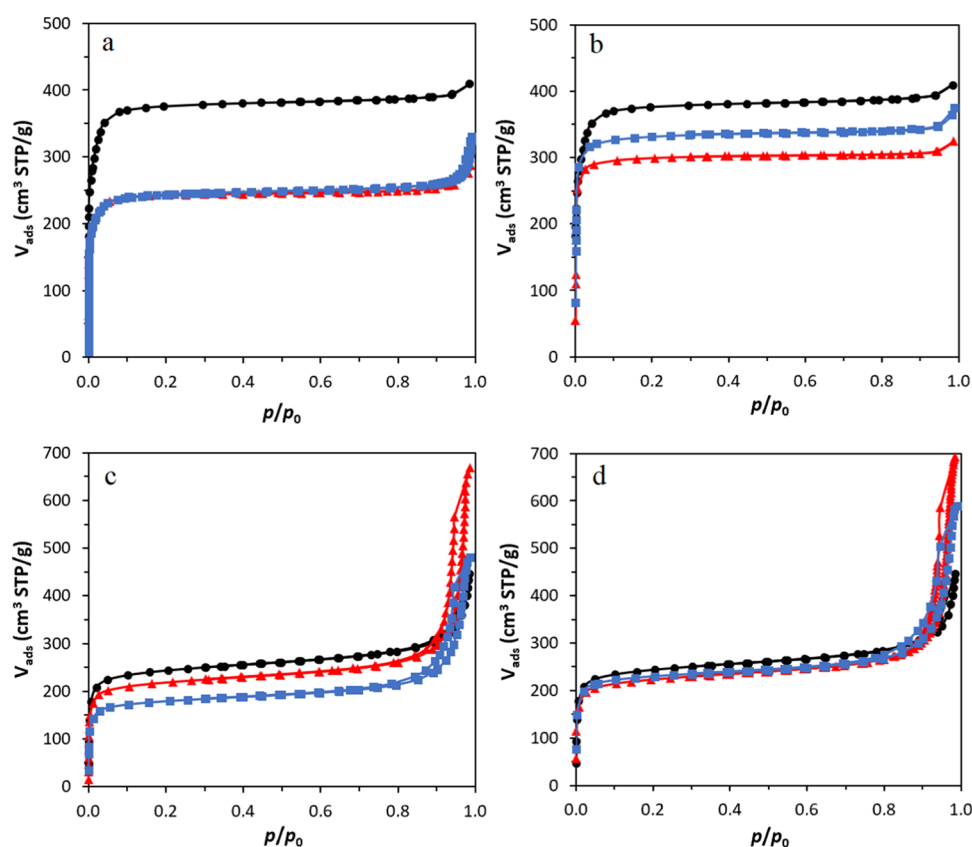
Figure 3. N_2 adsorption−desorption isotherms of (a) UiO-66 and UiO-66@HEC, (b) UiO-66 and UiO-66@chitosan, (c) UiO-66_NH_2 and UiO-66_NH_2@HEC, and (d) UiO-66_NH_2 and UiO-66_NH_2@chitosan: (black round) initial MOF powder, (red triangle) MOF@binder extrudates, and (blue square) MOF@binder granules.

processes do not affect UiO-66 and UiO-66_NH_2 frameworks owing to their high intrinsic mechanical stability.[34]

FTIR measurements were conducted to evaluate if the extrusion and spheronization processes affected the initial chemical properties of the UiO-66 and UiO-66_NH_2 powders. The resulting spectra of the MOF@binder extrudate and granule series are shown in Figure S10, and band assignment can be found elsewhere.[46] Namely, the most characteristic bands are found at 482 cm^{-1} (Zr-μ^3O symmetric stretching), 663 cm^{-1} (C−C−C aromatic ring), 1398 cm^{-1} (O−C−O symmetric stretching), and 1578 cm^{-1} (O−C−O asymmetric stretching). Additional bands at 1260 and 1386 cm^{-1} (C−N stretching) are characteristic of UiO-66_NH_2. They can all be superimposed with no additional emerging peak or clear differences of relative intensities, stressing that all solids have comparable chemical properties with their powder counterpart. Notably, a band at around 1650 cm^{-1} ($\nu_{C=O}$) is attributed to the presence of residual DMF. This band seems more intense in the case of UiO-66_NH_2-based materials, which correlates with the larger weight loss observed by TGA.

Nitrogen sorption isotherms of the MOF@binder extrudate and granule series are displayed in Figure 3 and compared to the initial UiO-66 and UiO-66_NH_2 powders. UiO-66-based materials are purely microporous, as deduced by their type I isotherm and absence of hysteresis. On the other hand, UiO-66_NH_2-based materials present a type I isotherm at low partial pressures ($p/p_0 < 0.2$) and a type IV isotherm at high partial pressures ($p/p_0 > 0.7$), along with a significant capillary hysteresis loop. This is classically observed in the case of microporous nanocrystals (crystals size <100 nm), offering a

considerable intercrystalline porosity upon agglomeration. This intercrystalline porosity seems promoted by the use of binders, leading to 2-fold higher mesopore volumes (V_{meso}) compared to the initial UiO-66_NH_2 powder. While there is no clear correlation between the binder nature or content and the resulting mesoporosity generated, the spheronization process seems to reduce the final mesoporosity by densifying the solids.

As reported in Table 1, lower BET surface areas and pore volumes are observed for the extrudates and granules—even when the proportion of organic binder (1.5−4.2 wt %) is taken into account. Previous studies reported a similar nonproportional decrease, attributed to partial pore blockage by the binders at 77 K.[47] Indeed, the UiO-66_NH_2-based solids shaped with less than 2.5 wt % of binder display a lower BET surface area loss (from −5 to −24%) than the UiO-66-based solids shaped with more than 2.5 wt % of binder (from −15 to −38%). One may note that except in the case of UiO-66_NH_2@HEC, all other MOF@binder granules display higher S_{BET} values than their extrudate counterparts. While it seems counterintuitive, the strong attrition exerted during spheronization may free some of the blocked porosity. Thus, and as indicated by the matching PXRD patterns and FTIR spectra, the shaping processes only have a small influence over the physicochemical properties of the final extrudates and granules including UiO-66 and UiO-66_NH_2, their impact being more pronounced on UiO-66-based solids, due to the larger content of binders, and on extrudates.

The compressive strength of the MOF@binder series was evaluated by crushing each time 10 extrudates or granules on
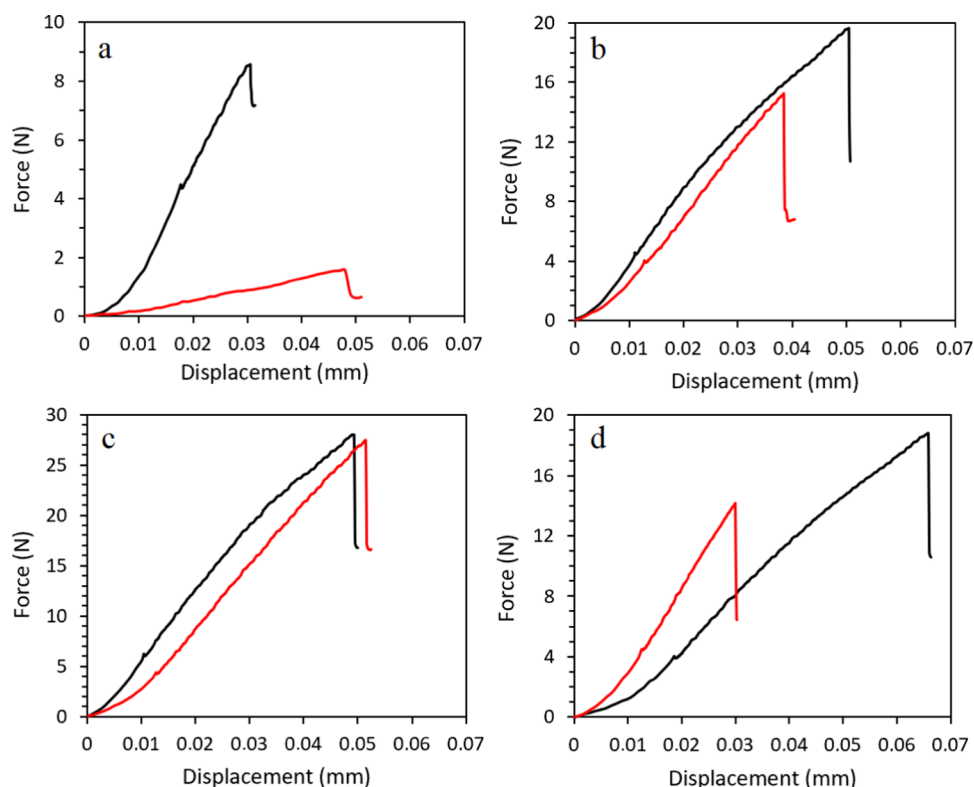
Figure 4. Representative force−displacement curves of (a) UiO-66@HEC, (b) UiO-66@chitosan, (c) UiO-66_NH$_2$@HEC, and (d) UiO-66_NH$_2$@chitosan: (black line) extrudates and (red line) granules.

their edge, and the results are given in Figure 4 and Table 1. The UiO-66@chitosan, UiO-66_NH$_2$@HEC, and UiO-66_NH$_2$@chitosan extrudates and granules all present a high compressive strength, with values exceeding 12 N of resistance before failure. However, the mechanical resistance of UiO-66@HEC extrudates and granules remains significantly lower than the other solids of the present study, while also having the most important BET surface area drop. Extrusion requires pastes with appropriate viscous properties to allow being conveyed along the screw and pushed through the die holes with minimal resistance. Too much resistance would induce a significant pressure increase, which could, in turn, affect the UiO-66 framework. Hence, an additional experiment using a co-binder—2 wt % of Ludox HS-40—was conducted. Silica colloids have already been used to prepare MOF granules[48] and would bring additional plasticizing properties for the extrusion step. Figure S11 presents the relating characterization of as-prepared UiO-66@HEC-Ludox extrudates and granules. A clear improvement of the compressive resistance is reached (*e.g.*, 12.7 *vs* 7.2 N for the extrudates), along with better-preserved BET surface area (1383 m^2/g: −8% compared to the initial UiO-66 powder), compared to UiO-66-HEC extrudates.

Hence, following extrusion and spheronization, highly robust and porous extrudates and granules were prepared. For comparison, following wet granulation, binderless granules made from UiO-66_NH$_2$ were observed with a resistance value of 0.3 N,[8] and UiO-66 granules formed with 5 wt % of mesoporous ρ-alumina binder displayed an average crushing strength of 4.7 N and a decrease of S_{BET} (−13%) in the range of the decreases reported herein.[35] A considerable improvement of the mechanical stability was thus obtained following this novel protocol, related to the presence of appropriate binders and the high bulk densities reached. Moreover, the

shaping protocol developed herein preserved most of the physicochemical properties of the initial UiO-66 and UiO-66_NH$_2$ powders, and especially the high BET surface area, which is a strong requirement for most applications involving porous MOF materials, especially for gas sorption. In particular, owing to its high retained S_{BET} along with the additional amino functions brought by the chitosan binder, UiO-66_NH$_2$@chitosan should be used for the capture of gaseous iodine.

Application of UiO-66 and UiO-66_NH$_2$-Based Granules for I_2 Capture. As a first hint of their potential for the remediation of radioactive iodine, the MOF@binder granule series were used in a fixed-bed setup and submitted to a constant flow of gaseous iodine at room temperature. The corresponding adsorption kinetic curves are shown in Figures 5
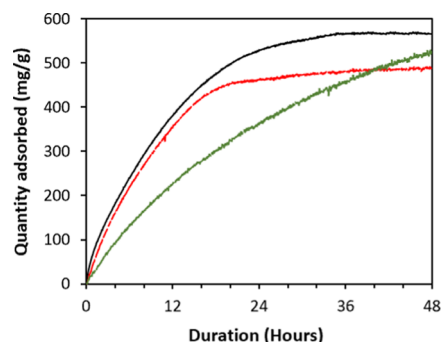

Figure 5. Iodine adsorption kinetic curves of UiO-66_NH$_2$-based materials: (black line) UiO-66_NH$_2$ powder, (red line) UiO-66_NH$_2$@HEC granules, and (green line) UiO-66_NH$_2$@chitosan granules.

Table 2. Quantity of Iodine Captured by UiO-66- and UiO-66_NH$_2$-Based Materials in Relation to Their BET Surface Area, and Their Related Kinetic Constants Data

sample	S_{BET} (m^2/g)	S_{BET} (%/powder)	$I_{2(ads)}$ (mg/g)	$I_{2(ads)}$ (%/powder)	k_{LDF} (h^{-1})[a]	R^2	t ($F = 0.9$) (h)[b]
UiO-66	1387	100	211	100	0.170	0.822	13.5
UiO-66@HEC	1006	67	148	66	0.224	0.979	10.3
UiO-66@chitosan	1291	85	190	84	0.151	0.943	15.2
UiO-66_NH$_2$	825	100	565	100	0.095	0.992	24.2
UiO-66_NH$_2$@HEC	683	83	481	85	0.111	0.994	20.7
UiO-66_NH$_2$@chitosan	878	106	527	93[c]	0.040	0.994	57.6

[a]Mass transfer coefficient from the linear drive force (LDF) model: $F(t) = 1 - \exp[-k_{LDF}t]$, where $F(t)$ is the fractional uptake. [b]Equilibration time t to reach 90% of the total adsorption capacity, from LDF fit. [c]Plateau not reached after 48 h.
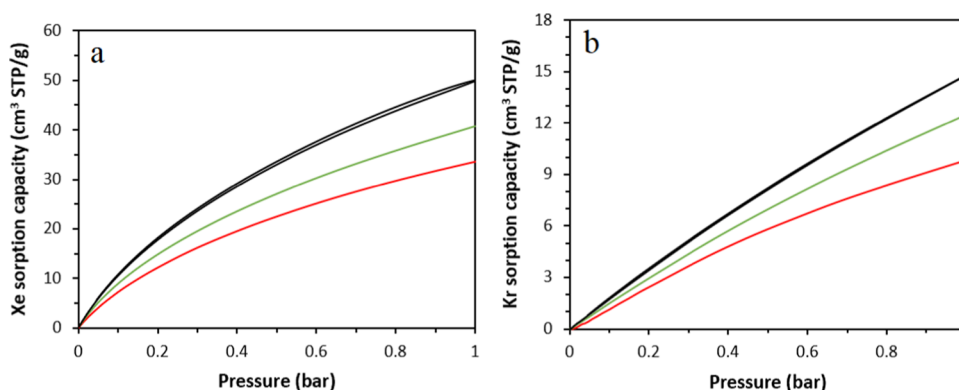

Figure 6. (a) Xenon and (b) krypton adsorption isotherms of UiO-66-based materials: (black) as-made powder, (red) UiO-66@HEC granules, and (green) UiO-66@chitosan granules.

and S12. As reported elsewhere, the UiO-66_NH$_2$-based materials present superior iodine adsorption capacity (565 vs 211 mg/g). Recently, the combination of experimentation and DFT calculations has shown the preferential interaction of molecular iodine with lone electron pair groups, including amino groups.[12] Of note, I_2 undergoes a kinetic conversion into anionic I_3^- within zirconium-based UiO-n MOFs, which is then slowly desorbed over time, thus highlighting that I_2 sorption is mostly governed by physisorption phenomena.[12]

Except UiO-66_NH$_2$@chitosan, all other MOF-based granules of the series reached their maximal uptake, characterized by a plateau, before 48 h. Intuitively, granules are expected to show greater diffusion restrictions as the MOF crystallites at the core of the granules would be harder to reach by iodine. Moreover, the latter might flow in between the granules bed, even if a rapid color change occurs (from white to purple) for all granules due to the effective capture of iodine within the pores of the MOFs (Figure S13), while the powder beds are denser in comparison. For practical comparisons between the materials, a simple analytic equation derived from the Linear Driving Force (LDF) model has been used for the kinetic curves.[49] This approach has been successfully applied to the study of adsorption kinetics of gaseous species in MOF materials.[50,51] The fitted and experimental curves can be observed in Figure S14. Of note, as the UiO-66 powder presents a second small but consistent uptake of iodine (measurement done twice), the resulting fitting is mediocre. This feature does not appear on the UiO-66-based shaped materials and could be related to different fluid dynamics within the adsorbent bed.

Table 2 summarizes the iodine adsorption capacity of the MOF@binder granule series and their powder counterparts, as well as the kinetic constants data. Especially, the granules present an adsorption capacity that is well correlated with the evolution of their BET surface area after extrusion and spheronization, as illustrated in Figure S15. This indicates that the amino groups of chitosan, as well as the hydroxy groups of both HEC and chitosan, have a negligible role over the total adsorption capacity toward molecular iodine, and further increasing their content would reduce the capacity of the materials. Of note, besides the presence of amino moieties in the UiO-66_NH$_2$ compound, the presence of chitosan also strongly reduces the mass transfer coefficient k_{LDF}, which is even more marked with UiO-66_NH$_2$ MOF. It is hypothesized that the amino groups of chitosan, located at the surface of the MOF crystals, weakly physisorbed some of the molecular iodine before releasing it back in the stream. According to the fit, its expected total I_2 adsorption capacity should be about 600 mg/g. Also, and as expected, the intercrystalline porosity deduced from N$_2$ isotherms does not seem to contribute to iodine encapsulation within the granules. Importantly, the prepared UiO-66_NH$_2$-based granules present I_2 adsorption capacities higher than 455 mg/g, which is the maximal capacity of silver-doped faujasite zeolites.[5] These granules are thus good candidates for further tests under realistic nuclear accidental conditions.

Application of UiO-66 and UiO-66_NH$_2$-Based Granules for Xe/Kr Adsorption. As a proof of the versatility of MOF composites for the nuclear energy field, the granules were also used for the adsorption of xenon and krypton gases. According to a computational study by Sikora et al., ideal MOF structures for Xe/Kr separation should present pore diameters from 4.1 Å—slightly larger than an atom of xenon (Xe$_{kinetic\ diameter}$ = 3.96 Å)—to 8.2 Å, hence favoring the creation of an induced dipole between the electronic cloud of the gas and the MOF frameworks, while the cavities should be

small enough to hold only one xenon atom.[52] The size of krypton atoms being smaller ($Kr_{kinetic\ diameter}$ = 3.60 Å), this gas would have less interactions. With tetrahedral cages of 7.5 Å and octahedral cages of 12 Å, connected through triangular windows of about 6 Å, the UiO-66 structure is a good candidate for xenon preferential capture over krypton.

By exploiting the xenon and krypton isotherms at room temperature, displayed in Figures 6 and S16, it is possible to estimate the xenon uptake and Xe/Kr selectivity of MOF composites. As expected, the adsorption capacity of the materials toward xenon and krypton is mostly dependent on their BET surface area,[15] with the best performing granular material here being the UiO-66@chitosan (S_{BET} = 1291 m^2/g). Moreover, both UiO-66_NH$_2$-based granules show lower Xe and Kr uptakes correlated to their lower BET surface area, implying that the amino functions do not provide interactions with the noble gases. Lee et al. reported higher xenon adsorption capacity on UiO-66_NH$_2$ (2.3 mmol/g) compared to UiO-66 (1.3 mmol/g), attributed to the ability of amino groups to polarize xenon preferentially.[53] This observation is not supported herein, as Figure S17 further highlights the linear relationship between the BET surface area and the adsorption capacity of the MOF-based materials. Table 3

Table 3. Xenon and Krypton Uptake Capacity of UiO-66- and UiO-66_NH$_2$-Based Materials at 1 bar and 293.15 K, and the Relative Xe/Kr Selectivity Predicted from the Ratio of Henry's Constants

sample	S_{BET} (m^2/g)	Xe$_{(ads)}$ (mmol/g)	Kr$_{(ads)}$ (mmol/g)	Xe/Kr selectivity
UiO-66	1510	2.01	0.66	7.0
UiO-66@HEC	1006	1.50	0.38	9.0
UiO-66@chitosan	1291	1.63	0.48	8.1
UiO-66_NH$_2$	925	1.35	0.35	7.7
UiO-66_NH$_2$@HEC	683	1.20	0.34	7.1
UiO-66_NH$_2$@chitosan	878	1.26	0.32	8.3

summarizes the uptake capacity of the materials issued from the isotherms as well as the corresponding Xe/Kr adsorption selectivity, obtained from the ratio of Henry's constants. The as-made UiO-66 powder exhibits a predicted Xe/Kr selectivity of 7.0, in line with the literature (7.2).[53] Importantly, the presence of binders seems to improve this selectivity, with performances of the UiO-66-based granules (8.1−9.0) higher than their powder counterpart. For comparison, a leading MOF-based material for Xe/Kr separation is the HKUST-1 compound, displaying a predicted Xe/Kr selectivity of 8.4 under the same conditions.[7] However, its structure is far less stable over time. This improvement may be attributed to a reduction of the flexibility of the MOF frameworks by the binders, especially at low pressures (in a range where Henry's constants are calculated),[54] or to partial pore blockage, thus reducing the interactions with Kr molecules. Hence, the use of binders could be a good strategy to orientate the separation selectivity of MOFs.

CONCLUSIONS

For the first time, an extrusion-spheronization process has been applied to MOF materials, namely, UiO-66 and UiO-66_NH$_2$. To ensure sufficient robustness of the final objects, up to 6 wt % of a biosourced binder, either chitosan or 2-hydroxymethyl cellulose (HEC), has been added. The obtained extrudates and

granules present similar physicochemical properties to the initial UiO-66 and UiO-66_NH$_2$ powders, therefore implying that this process is suited for the shaping of MOFs from the UiO-66 family and could be applied more broadly to other MOF structures. We pointed out that the presence of a binder lowers the BET surface area in a nonlinear manner (5−38% of S_{BET} reduction for 2.0−5.6 wt % of binder), as typically observed, but it also favors the generation of intercrystalline pores when the crystallites are small enough—in this case with UiO-66_NH$_2$. Importantly, the as-produced extrudates and granules present a significant mechanical resistance toward compression, in the range of 7−20 N. When an insufficient mechanical resistance is achieved, as in the case of UiO-66 with 5.0 wt % of HEC, the addition of a co-binder, colloidal silica, further improves it (from 7.2 to 12.7 N) while lowering the impact of the process over the BET surface area (from −38 to −8% of S_{BET} compared to the initial powder) by acting as a plasticizer.

The series of shaped UiO-66 and UiO-66_NH$_2$-based granules were further applied to the capture of iodine. UiO-66_NH$_2$-based granules reached the highest iodine uptake, above 480 mg/g after 48 h independently of the binder used. This is in line with the commercial adsorbent used nowadays (silver-doped faujasite zeolite, 455 mg/g). Finally, these granules were also utilized for the adsorption of xenon and krypton, with gas uptakes mostly correlated to their BET surface area. Hence, the UiO-66-based granules presented the highest uptakes, while the predicted Xe/Kr uptake ratio (7.1−9.0) was similar for all materials. Finally, it was observed that the presence of binders might slightly improve the Xe/Kr selectivity.

Hence, the produced MOF-based granules retained most of the performance of the initial MOF UiO-66 and UiO-66_NH$_2$ powders. Their use in a demonstrator under realistic conditions would be of interest, in particular to evaluate the impact of the presence of binders on the long-term stability of the shaped materials. Also, the broader application of this shaping technique to other attractive MOF structures is envisaged.

ASSOCIATED CONTENT

Ⓢ Supporting Information

The Supporting Information is available free of charge at https://pubs.acs.org/doi/10.1021/acsami.1c21380.

> Additional experimental details; photographs of extrusion process and iodine capture test; SEM micrographs of MOF powders, extrudates, and granules; TGA thermographs, FTIR spectra, N$_2$ adsorption−desorption isotherms, PXRD patterns, and representative force−displacement curves for all materials; iodine adsorption curves for UiO-66-based materials; fitted iodine adsorption kinetic curves; xenon and krypton adsorption−desorption isotherms for UiO-66_NH$_2$-based materials; and correlation curves between the BET surface area and the performance of all materials (PDF)

AUTHOR INFORMATION

Corresponding Author

Jérémy Dhainaut − *Univ. Lille, CNRS, Centrale Lille, Univ. Artois, UMR 8181 - UCCS - Unité de Catalyse et Chimie du Solide, F-59000 Lille, France;* ⓞ orcid.org/0000-0002-1035-0114; Email: jeremy.dhainaut@univ-lille.fr

Authors

Alla Abramova − *Univ. Lille, CNRS, INRA, Centrale Lille, Univ. Artois, FR 2638 − IMEC − Institut Michel-Eugène Chevreul, F-59000 Lille, France*

Nelly Couzon − *Univ. Lille, CNRS, Centrale Lille, Univ. Artois, UMR 8181 - UCCS - Unité de Catalyse et Chimie du Solide, F-59000 Lille, France;* orcid.org/0000-0002-8539-3290

Maëva Leloire − *Univ. Lille, CNRS, Centrale Lille, Univ. Artois, UMR 8181 - UCCS - Unité de Catalyse et Chimie du Solide, F-59000 Lille, France; Institut de Radioprotection et de Sureté Nucléaire (IRSN), PSN-RES/SEREX, Saint-Paul Lez Durance 13115, France*

Philippe Nerisson − *Institut de Radioprotection et de Sureté Nucléaire (IRSN), PSN-RES/SEREX, Saint-Paul Lez Durance 13115, France*

Laurent Cantrel − *Institut de Radioprotection et de Sureté Nucléaire (IRSN), PSN-RES/SEREX, Saint-Paul Lez Durance 13115, France*

Sébastien Royer − *Univ. Lille, CNRS, Centrale Lille, Univ. Artois, UMR 8181 - UCCS - Unité de Catalyse et Chimie du Solide, F-59000 Lille, France;* orcid.org/0000-0002-5635-0144

Thierry Loiseau − *Univ. Lille, CNRS, Centrale Lille, Univ. Artois, UMR 8181 - UCCS - Unité de Catalyse et Chimie du Solide, F-59000 Lille, France;* orcid.org/0000-0001-8175-3407

Christophe Volkringer − *Univ. Lille, CNRS, Centrale Lille, Univ. Artois, UMR 8181 - UCCS - Unité de Catalyse et Chimie du Solide, F-59000 Lille, France;* orcid.org/0000-0003-2769-9360

Complete contact information is available at:
https://pubs.acs.org/10.1021/acsami.1c21380

Author Contributions

J.D, T.L., and C.V. conceived and designed the project. S.R. and J.D. acquired funding. J.D. prepared the MOF powders. A.A. shaped the materials. A.A. and J.D. conducted all characterizations. M.L., N.C., and J.D. measured I_2 adsorption. N.C. measured Kr and Xe isotherms. A.A. and J.D. analyzed the data. J.D. wrote the manuscript. All authors discussed the results and commented on the manuscript.

Notes

The authors declare no competing financial interest.

■ REFERENCES

(1) Bal, M.; Jose, R. C.; Meikap, B. C. Control of Accidental Discharge of Radioactive Materials by Filtered Containment Venting System: A Review. *Nucl. Eng. Technol.* **2019**, *51*, 931−942.

(2) Mathieu, A.; Kajino, M.; Korsakissok, I.; Périllat, R.; Quélo, D.; Quérel, A.; Saunier, O.; Sekiyama, T. T.; Igarashi, Y.; Didier, D. Fukushima Daiichi-Derived Radionuclides in the Atmosphere, Transport and Deposition in Japan: A Review. *Appl. Geochem.* **2018**, *91*, 122−139.

(3) Tronko, M. D.; Howe, G. R.; Bogdanova, T. I.; Bouville, A. C.; Epstein, O. V.; Brill, A. B.; Likhtarev, I. A.; Fink, D. J.; Markov, V. V.; Greenebaum, E.; Olijnyk, V. A.; Masnyk, I. J.; Shpak, V. M.; McConnell, R. J.; Tereshchenko, V. P.; Robbins, J.; Zvinchuk, O. V.; Zablotska, L. B.; Hatch, M.; Luckyanov, N. K.; Ron, E.; Thomas, T. L.; Voillequé, P. G.; Beebe, G. W. A Cohort Study of Thyroid Cancer and Other Thyroid Diseases After the Chornobyl Accident: Thyroid Cancer in Ukraine Detected During First Screening. *J. Natl. Cancer Inst.* **2006**, *98*, 897−903.

(4) Leroy, O.; Monsanglant-Louvet, C. Trapping Measurements of Volatile Iodine by Sand Bed and Metallic Filters. *J. Radioanalytical Nucl. Chem.* **2019**, *322*, 913−922.

(5) Azambre, B.; Chebbi, M.; Leroy, O.; Cantrel, L. Effects of Zeolitic Parameters and Irradiation on the Retention Properties of Silver Zeolites Exposed to Molecular Iodine. *Ind. Eng. Chem. Res.* **2018**, *57*, 1468−1479.

(6) Chebbi, M.; Chibani, S.; Paul, J.-F.; Cantrel, L.; Badawi, M. Evaluation of Volatile Iodine Trapping in Presence of Contaminants: A Periodic DFT Study on Cation-Exchanged-Faujasite. *Micro. Meso. Mater.* **2017**, *239*, 111−122.

(7) Huve, J.; Ryzhikov, A.; Nouali, H.; Lalia, V.; Augé, G.; Daou, T. J. Porous Sorbents for the Capture of Radioactive Iodine Compounds: A Review. *RSC Adv.* **2018**, *8*, 29248−29273.

(8) Leloire, M.; Dhainaut, J.; Devaux, P.; Leroy, O.; Desjonqueres, H.; Poirier, S.; Nerisson, P.; Cantrel, L.; Royer, S.; Loiseau, T.; Volkringer, C. Stability and Radioactive Gaseous Iodine-131 Retention Capacity of Binderless UiO-66_NH₂ Granules Under Severe Nuclear Accidental Conditions. *J. Hazard. Mater.* **2021**, *416*, No. 125890.

(9) Lee, H. C.; Lee, D. Y.; Kim, H. S.; Kim, C. R. Performance Evaluation of TEDA Impregnated Activated Carbon under Long Term Operation Simulated NPP Operating Conditions. *Nucl. Eng. Technol.* **2020**, *52*, 2652−2659.

(10) Sava, D. F.; Rodriguez, M. A.; Chapman, K. W.; Chupas, P. J.; Greathouse, J. A.; Crozier, P. S.; Nenoff, T. M. Capture of Volatile Iodine, a Gaseous Fission Product, by Zeolitic Imidazolate Framework-8. *J. Am. Chem. Soc.* **2011**, *133*, 12398−12401.

(11) Falaise, C.; Volkringer, C.; Facqueur, J.; Bousquet, T.; Gasnot, L.; Loiseau, T. Capture of Iodine in Highly Stable Metal-Organic Frameworks: A Systematic Study. *Chem. Commun.* **2013**, *49*, 10320−10322.

(12) Leloire, M.; Walshe, C.; Devaux, P.; Giovine, R.; Duval, S.; Bousquet, T.; Chibani, S.; Paul, J.-P.; Moissette, A.; Vezin, H.; Nerisson, P.; Cantrel, L.; Volkringer, C.; Loiseau, C. Capture of Gaseous Iodine in Isoreticular Zirconium-based UiO-n Metal-Organic Frameworks: Influence of Amino Functionalization, DFT Calculations, Raman and EPR Spectroscopic Investigations. *Chem. - Eur. J.* **2022**, No. e202104437.

(13) Marshall, R. J.; Griffin, S. L.; Wilson, C.; Forgan, R. S. Stereoselective Halogenation of Integral Unsaturated C-C bonds in Chemically and Mechanically Robust Zr and Hf MOFs. *Chem. - Eur. J.* **2016**, *22*, 4870−4877.

(14) Jelea, A. An Equation of State for Xenon/Krypton Mixtures Confined in the Nuclear Fuels. *J. Nucl. Mater.* **2020**, *530*, No. 151952.

(15) Banerjee, D.; Simon, C. M.; Elsaidi, S. K.; Haranczyk, M.; Thallapally, P. K. Xenon Gas Separation and Storage Using Metal-Organic Frameworks. *Chem* **2018**, *4*, 466−494.

(16) Thallapally, P. K.; Grate, J. W.; Motkuri, R. K. Facile Xenon Capture and Release at Room Temperature using a Metal-Organic Framework: A Comparison with Activated Charcoal. *Chem. Commun.* **2012**, *48*, 347−349.

(17) Jameson, C. J.; Jameson, A. K.; Lim, H. M. Competitive Adsorption of Xenon and Krypton in Zeolite NaA: Xe-129 Nuclear Magnetic Resonance Studies and Grand Canonical Monte Carlo Simulations. *J. Chem. Phys.* **1997**, *107*, 4364−4372.

(18) Daniel, C.; Elbaraoui, A.; Aguado, S.; Springuel-Huet, M. A.; Nossov, A.; Fontaine, J. P.; Topin, S.; Taffary, T.; Deliere, L.;

Schuurman, Y.; Farrusseng, D. Xenon Capture on Silver-Loaded Zeolites: Characterization of Very Strong Adsorption Sites. *J. Phys. Chem. C* **2013**, *117*, 15122−15129.

(19) Banerjee, D.; Simon, C. M.; Plonka, A. M.; Motkuri, R. K.; Liu, J.; Chen, X.; Smit, B.; Parise, J. B.; Haranczyk, M.; Thallapally, P. K. Metal-Organic Framework with Optimally Selective Xenon Adsorption and Separation. *Nat. Commun.* **2016**, *7*, No. 11831.

(20) Perry, J. J., IV; Teich-McGoldrick, S. L.; Meek, S. T.; Greathouse, J. A.; Haranczyk, M.; Allendorf, M. D. Noble Gas Adsorption in Metal-Organic Frameworks Containing Open Metal Sites. *J. Phys. Chem. C* **2014**, *118*, 11685−11698.

(21) Mueller, U.; Schubert, M.; Teich, F.; Puetter, H.; Schierle-Arndt, K.; Pastré, J. Metal-Organic Frameworks-Prospective Industrial Applications. *J. Mater. Chem.* **2006**, *16*, 626−636.

(22) Howarth, A. J.; Liu, Y.; Li, P.; Li, Z.; Wang, T. C.; Hupp, J. T.; Farha, O. K. Chemical, Thermal and Mechanical Stabilities of Metal-Organic Frameworks. *Nat. Rev.* **2016**, *1*, No. 15018.

(23) Cavka, J. H.; Jakobsen, S.; Olsbye, U.; Guillou, N.; Lamberti, C.; Bordiga, S.; Lillerud, K. P. A New Zirconium Inorganic Building Brick Forming Metal Organic Frameworks with Exceptional Stability. *J. Am. Chem. Soc.* **2008**, *130*, 13850−13851.

(24) Chen, Z.; Hanna, S. L.; Redfern, L. R.; Alezi, D.; Islamoglu, T.; Farha, O. K. Reticular Chemistry in the Rational Synthesis of Functional Zirconium Cluster-based MOFs. *Coord. Chem. Rev.* **2019**, *386*, 32−49.

(25) Falaise, C.; Volkringer, C.; Vigier, J.-F.; Henry, N.; Beaurain, A.; Loiseau, T. Three-Dimensional MOF-Type Architectures with Tetravalent Uranium Hexanuclear Motifs (U_6O_8). *Chem. - Eur. J.* **2013**, *19*, 5324−5331.

(26) Falaise, C.; Charles, J.-S.; Volkringer, C.; Loiseau, T. Thorium Terephtalates Coordination Polymers Synthesized in Solvothermal DMF/H_2O System. *Inorg. Chem.* **2015**, *54*, 2235−2242.

(27) Martin, N. P.; März, J.; Feuchter, H.; Duval, S.; Roussel, P.; Henry, N.; Ikeda-Ohno, A.; Loiseau, T.; Volkringer, C. Synthesis and Structural Characterization of the First Neptunium based Metal-Organic Frameworks Incorporating {Np_6O_8} Hexanuclear Clusters. *Chem. Commun.* **2018**, *54*, 6979−6982.

(28) Bai, Y.; Dou, Y.; Xie, L.-H.; Rutledge, W.; Li, J.-R.; Zhou, H.-C. Zr-based Metal-Organic Frameworks: Design, Synthesis, Structure, and Applications. *Chem. Soc. Rev.* **2016**, *45*, 2327−2367.

(29) Xie, W.; Cui, D.; Zhang, S. R.; Xu, Y. H.; Jiang, D. L. Iodine Capture in Porous Organic Polymers and Metal-Organic Frameworks Materials. *Mater. Horiz.* **2019**, *6*, 1571−1595.

(30) Peterson, G. W.; Mahle, J. J.; DeCoste, J. B.; Gordon, W. O.; Rossin, J. A. Extraordinary NO_2 Removal by the Metal-Organic Framework UiO-66_NH_2. *Angew. Chem., Int. Ed.* **2016**, *55*, 6235−6238.

(31) Browe, M. A.; Napolitano, A.; DeCoste, J. B.; Peterson, G. W. Filtration of Chlorine and Hydrogen Chloride Gas by Engineered UiO-66_NH_2 Metal-Organic Framework. *J. Hazard. Mater.* **2017**, *332*, 162−167.

(32) Cmarik, G. E.; Kim, M.; Cohen, S. M.; Walton, K. S. Tuning the Adsorption Properties of UiO-66 via Ligand Functionalization. *Langmuir* **2012**, *28*, 15606−15613.

(33) Yeskendir, B.; Dacquin, J.-P.; Lorgouilloux, Y.; Courtois, C.; Royer, S.; Dhainaut, J. From Metal-Organic Framework Powders to Shaped Solids: Recent Developments and Challenges. *Mater. Adv.* **2021**, *2*, 7139−7186.

(34) Dhainaut, J.; Avci-Camur, C.; Troyano, J.; Legrand, A.; Canivet, J.; Imaz, I.; Maspoch, D.; Reinsch, H.; Farrusseng, D. Systematic Study of the Impact of MOF Densification into Tablets on Textural and Mechanical Properties. *CrystEngComm* **2017**, *19*, 4211−4218.

(35) Valekar, A. H.; Cho, K.-H.; Lee, U.-H.; Lee, J. S.; Yoon, J. W.; Hwang, Y. K.; Lee, S. G.; Cho, S. J.; Chang, J.-S. Shaping of Porous Metal-Organic Framework Granules using Mesoporous ρ-Alumina as a Binder. *RSC Adv.* **2017**, *7*, 55767−55777.

(36) Chanut, N.; Wiersum, A. D.; Lee, U.; Hwang, K.; Ragon, F.; Chevreau, H.; Bourrelly, S.; Kuchta, B.; Chang, J.; Serre, C.; Llewellyn, P. L. Observing the Effects of Shaping on Gas Adsorption

in Metal- Organic Frameworks. *Eur. J. Inorg. Chem.* **2016**, *2016*, 4416−4423.

(37) Ren, J.; Musyoka, N. M.; Langmi, H. W.; Swartbooi, A.; North, B. C.; Mathe, M. A More Efficient Way to Shape Metal-Organic Framework (MOF) Powder Materials for Hydrogen Storage Applications. *Int. J. Hydrog. Energy* **2015**, *40*, 4617−4622.

(38) Khabzina, Y.; Dhainaut, J.; Ahlhelm, M.; Richter, H.-J.; Reinsch, H.; Stock, N.; Farrusseng, D. Synthesis and Shaping Scale-up Study of Functionalized UiO-66 MOF for Ammonia Air Purification Filters. *Ind. Eng. Chem. Res.* **2018**, *57*, 8200−8208.

(39) Brugnerotto, J.; Lizardi, J.; Goycoolea, F. M.; Argüelles-Monal, W.; Desbrières, J.; Rinaudo, M. An Infrared Investigation in Relation with Chitin and Chitosan Characterization. *Polymer* **2001**, *42*, 3569−3580.

(40) Petrovick, G. F.; Breitkreutz, J. Spheronization of Solid Lipid Extrudates: Elucidation of Spheroid Formation Mechanism. *Eur. J. Pharm. Biopharm.* **2018**, *125*, 148−158.

(41) Sohn, H. Y.; Moreland, C. The Effect of Particle Size Distribution on Packing Density. *Can. J. Chem. Eng.* **1968**, *46*, 162−167.

(42) Hong, W. Y.; Perera, S. P.; Burrows, A. D. Manufacturing of Metal-Organic Framework Monoliths and their Application in CO_2 Adsorption. *Micro. Meso. Mater.* **2015**, *214*, 149−155.

(43) Cheng, H.; Høeg Hansen, J.; Tolderlund Rasmussen, H. A General Extrudate Bulk Density Model for both Twin-Screw and Single-Screw Extruder Extrusion Cooking Processes. *J. Food. Eng.* **2010**, *78*, 10−19.

(44) Shearer, G. C.; Forselv, S.; Chavan, S.; Bordiga, S.; Mathisen, K.; Bjørgen, M.; Svelle, S.; Lillerud, K. P. In Situ Infrared Spectroscopic and Gravimetric Characterisation of the Solvent Removal and Dehydroxylation of the Metal Organic Frameworks UiO-66 and UiO-67. *Topics Catal.* **2013**, *56*, 770−782.

(45) Kaya, M.; Mujtaba, M.; Ehrlich, H.; Salaberria, A. M.; Baran, T.; Amemiya, C. T.; Galli, R.; Akyuz, L.; Sargin, I.; Labidi, J. On Chemistry of γ-Chitin. *Carbohydr. Polym.* **2017**, *176*, 177−186.

(46) Valenzano, L.; Civalleri, B.; Chavan, S.; Bordiga, S.; Nilsen, M. H.; Jakobsen, S.; Lillerud, K. P.; Lamberti, C. Disclosing the Complex Structure of UiO-66 Metal Organic Framework: A Synergic Combination of Experiment and Theory. *Chem. Mater.* **2011**, *23*, 1700−1718.

(47) Dhainaut, J.; Bonneau, M.; Ueoka, R.; Kanamori, K.; Furukawa, S. Formulation of Metal-Organic Framework Inks for the 3D Printing of Robust Microporous Solids Toward High-Pressure Gas Storage and Separation. *ACS Appl. Mater. Interfaces* **2020**, *12*, 10983−10992.

(48) Kim, P.; You, Y.; Park, H.; Chang, J.; Bae, Y.; Lee, C.; Suh, J. Separation of SF_6 from SF_6/N_2 Mixture using Metal-Organic Framework MIL-100(Fe) Granule. *Chem. Eng. J.* **2015**, *262*, 683−690.

(49) Sircar, S.; Hufton, J. R. Why does the Linear Driving Force Model for Adsorption Kinetics Work? *Adsorption* **2000**, *6*, 137−147.

(50) Blǎnitǎ, G.; Streza, M.; Lazǎr, M. D.; Lupu, D. Kinetics of Hydrogen Adsorption in MIL-101 Single Pellets. *Int. J. Hydrogen Energy* **2017**, *42*, 3064−3077.
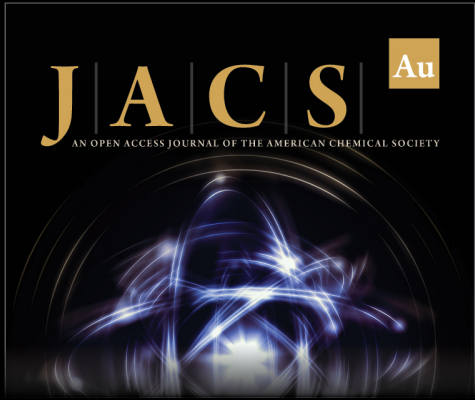
(51) Streza, M.; Grad, O.; Lazǎr, M. D.; Depriester, M.; Longuemart, S.; Sahraoui, A. H.; Blǎnitǎ, G.; Lupu, D. Hybrid MOFs-Graphene Composites: Correlation Between Thermal Transport and Kinetics of Hydrogen Adsorption. *Int. J. Heat Mass. Transfer* **2019**, *143*, No. 118539.

(52) Sikora, B. J.; Wilmer, C. E.; Greenfield, M. L.; Snurr, R. Q. Thermodynamic Analysis of Xe/Kr Selectivity in over 137 000 Hypothetical Metal-Organic Frameworks. *Chem. Sci.* **2012**, *3*, 2217−2223.

(53) Lee, S.-J.; Yoon, T.-U.; Kim, A.-R.; Kim, S.-Y.; Cho, K.-H.; Hwang, Y. K.; Yeon, J.-W.; Bae, Y.-S. Adsorptive Separation of Xenon/Krypton Mixtures using a Zirconium-based Metal-Organic Framework with High Hydrothermal and Radioactive Stabilities. *J. Hazardous Mater.* **2016**, *320*, 513−520.

(54) Kriesten, M.; Schmitz, J. V.; Siegel, J.; Smith, C. E.; Kaspereit, M.; Hartmann, M. Shaping of Flexible Metal-Organic Frameworks:

Combining Macroscopic Stability and Framework Flexibility. *Eur. J. Inorg. Chem.* **2019**, *2019*, 4700−4709.